The Astronomical Journal, 160:133 (13pp), 2020 September https://doi.org/10.3847/1538-3881/aba526

TOI 694b and TIC 220568520b: Two Low-mass Companions near the Hydrogen-burning Mass Limit Orbiting Sun-like Stars

Ismael Mireles[1], Avi Shporer[1], Nolan Grieves[2], George Zhou[3], Maximilian N. Günther[1,22], Rafael Brahm[4,5], Carl Ziegler[6], Keivan G. Stassun[7], Chelsea X. Huang[1], Louise Nielsen[2], Leonardo A. dos Santos[2], Stéphane Udry[2], François Bouchy[2], Michael Ireland[8], Alexander Wallace[8], Paula Sarkis[9], Thomas Henning[9], Andrés Jordán[4,5], Nicholas Law[10], Andrew W. Mann[10], Leonardo A. Paredes[11], Hodari-Sadiki James[11], Wei-Chun Jao[11], Todd J. Henry[12], R. Paul Butler[13], Joseph E. Rodriguez[14], Liang Yu[1], Erin Flowers[15,23], George R. Ricker[1], David W. Latham[3], Roland Vanderspek[1], Sara Seager[1,16,17], Joshua N. Winn[15], Jon M. Jenkins[18], Gabor Furesz[1], Katharine Hesse[19], Elisa V. Quintana[20], Mark E. Rose[18], Jeffrey C. Smith[18,21], Peter Tenenbaum[18,21], Michael Vezie[16], Daniel A. Yahalomi[3], and Zhuchang Zhan[16]

[1] Department of Physics and Kavli Institute for Astrophysics and Space Research, Massachusetts Institute of Technology, Cambridge, MA 02139, USA
[2] Observatoire astronomique de l'Université de Genève, 51 Chemin des Maillettes, 1290 Versoix, Switzerland
[3] Harvard-Smithsonian Center for Astrophysics, 60 Garden Street, Cambridge, MA 02138, USA
[4] Facultad de Ingeniería y Ciencias, Universidad Adolfo Ibáñez, Av. Diagonal las Torres 2640, Peñalolén, Santiago, Chile
[5] Millennium Institute for Astrophysics, Chile
[6] Dunlap Institute for Astronomy and Astrophysics, University of Toronto, 50 St. George Street, Toronto, Ontario M5S 3H4, Canada
[7] Vanderbilt University, Department of Physics & Astronomy, 6301 Stevenson Center Lane, Nashville, TN 37235, USA
[8] Research School of Astronomy and Astrophysics, Australian National University, Canberra, ACT 2611, Australia
[9] Max-Planck-Institut für Astronomie, Königstuhl 17, D-69117 Heidelberg, Germany
[10] Department of Physics and Astronomy, The University of North Carolina at Chapel Hill, Chapel Hill, NC 27599-3255, USA
[11] Physics and Astronomy Department, Georgia State University, Atlanta, GA 30302, USA
[12] RECONS Institute, Chambersburg, PA, USA
[13] Earth & Planets Laboratory, Carnegie Institution for Science, 5241 Broad Branch Road, NW, Washington, DC 20015, USA
[14] Center for Astrophysics | Harvard & Smithsonian, 60 Garden Street, Cambridge, MA 02138, USA
[15] Department of Astrophysical Sciences, Princeton University, Princeton, NJ 08544, USA
[16] Department of Earth, Atmospheric, and Planetary Sciences, Massachusetts Institute of Technology, Cambridge, MA 02139, USA
[17] Department of Aeronautics and Astronautics, MIT, 77 Massachusetts Avenue, Cambridge, MA 02139, USA
[18] NASA Ames Research Center, Moffett Field, CA 94035, USA
[19] Department of Astronomy, Wesleyan University, Middletown, CT 06459, USA
[20] NASA Goddard Space Flight Center, 8800 Greenbelt Road, Greenbelt, MD 20771, USA
[21] SETI Institute, Mountain View, CA 94043, USA
Received 2020 May 15; revised 2020 July 3; accepted 2020 July 9; published 2020 August 26

Abstract

We report the discovery of TOI 694 b and TIC 220568520 b, two low-mass stellar companions in eccentric orbits around metal-rich Sun-like stars, first detected by the Transiting Exoplanet Survey Satellite (TESS). TOI 694 b has an orbital period of 48.05131 ± 0.00019 days and eccentricity of 0.51946 ± 0.00081, and we derive a mass of 89.0 ± 5.3 $M_{\rm Jup}$ (0.0849 ± 0.0051 $M_{\odot}$) and radius of 1.111 ± 0.017 $R_{\rm Jup}$ (0.1142 ± 0.0017 $R_{\odot}$). TIC 220568520 b has an orbital period of 18.55769 ± 0.00039 days and eccentricity of 0.0964 ± 0.0032, and we derive a mass of 107.2 ± 5.2 $M_{\rm Jup}$ (0.1023 ± 0.0050 $M_{\odot}$) and radius of 1.248 ± 0.018 $R_{\rm Jup}$ (0.1282 ± 0.0019 $R_{\odot}$). Both binary companions lie close to and above the hydrogen-burning mass threshold that separates brown dwarfs and the lowest-mass stars, with TOI 694 b being 2σ above the canonical mass threshold of 0.075 $M_{\odot}$. The relatively long periods of the systems mean that the magnetic fields of the low-mass companions are not expected to inhibit convection and inflate the radius, which according to one leading theory is common in similar objects residing in short-period tidally synchronized binary systems. Indeed we do not find radius inflation for these two objects when compared to theoretical isochrones. These two new objects add to the short but growing list of low-mass stars with well-measured masses and radii, and highlight the potential of the TESS mission for detecting such rare objects orbiting bright stars.

Unified Astronomy Thesaurus concepts: Low mass stars (2050); M dwarf stars (982); Eclipsing binary stars (444)

1. Introduction

The stellar initial mass function shows a maximum at or close to 0.1 $M_{\odot}$, at the bottom of the main sequence (see, e.g., Chabrier 2003; Bonnell et al. 2007; Andersen et al. 2008; Krumholz 2014, and references therein). That, combined with the increase in main-sequence lifetime with decreasing stellar mass means that stars around 0.1 $M_{\odot}$ are the most abundant stars in the galaxy. However, despite their abundance the precise measurement of their stellar properties, specifically radius and mass, is hindered by their low luminosity, leading to only a small number of objects at ∼0.1 $M_{\odot}$ with precisely measured radius and mass.

Precise measurements of those properties are desirable, for example, when low-mass stars are found to host planets, since the precision of the measured planet parameters depends on the precision of the host star parameters. The latter is especially relevant to low-mass stars since their small radius and mass provides an opportunity to detect smaller planets orbiting them

[22] Juan Carlos Torres Fellow.
[23] NSF Graduate Research Fellow.

compared to larger, Sun-like stars (this is commonly known as the "M-dwarf opportunity"; see, e.g., Gould et al. 2003; Nutzman & Charbonneau 2008).

One way to detect such low-mass stars whose mass and radius can be precisely measured is through wide-field photometric transit surveys. The signal searched for in those surveys scales quadratically with the radius of the transiting object, and the radius of the smallest stars is the same as that of gas-giant planets, resulting in similar signals. This was already exemplified by several discoveries (e.g., Pont et al. 2005a; Díaz et al. 2014; Zhou et al. 2014b; Chaturvedi et al. 2016; von Boetticher et al. 2019).

A comparison between the sizes and masses of low-mass stars to theoretical predictions has shown that the measured stellar radii tend to be larger than expected (e.g., Ribas 2006; Torres et al. 2010; Kesseli et al. 2018) by about 5%–10%. The leading hypothesis for the inflated stellar radius is strong magnetic fields that inhibit convection, leading to decreased heat flow and in turn increased radius (Chabrier et al. 2007). The magnetic fields are strengthened by the relatively fast stellar rotation resulting from spin–orbit tidal synchronization in short orbital period systems (Mazeh 2008). Given that these systems are detected through photometric transit surveys it is not surprising they tend to have short periods (shorter than $\sim$10 days).

Here we present the discovery of two longer-period eclipsing binary systems with low-mass companions close to 0.1 $M_{\odot}$ detected by the Transiting Exoplanet Survey Satellite (TESS; Ricker et al. 2015) mission: TOI 694 b, with a period of 48.1 days, and TIC 220568520 b, with a period of 18.6 days. The long orbital periods mean that the companions are not expected to be tidally synchronized, so they are not expected to rotate rapidly and their magnetic fields are not expected to be strong enough to impact the stellar radius. We describe the TESS and ground-based observations in Section 2, and the data analysis in Section 3. We discuss our results in Section 4 and conclude with a summary in Section 5.

2. Observations

Basic photometric and astrometric information about the two targets studied here is given in Table 1.

Table 1
Target Information

Parameter	TOI 694	TIC 220568520	Source
TIC	55383975	220568520	TIC V8[a]
R.A.	05:09:32.06	03:05:08.58	Gaia DR2[b]
Decl.	−64:01:33.9	−62:51:24.56	Gaia DR2[b]
$\mu_{\rm R.A.}$ (mas yr^{-1})	6.468 ± 0.044	16.381 ± 0.038	Gaia DR2[b]
$\mu_{\rm Decl.}$ (mas yr^{-1})	25.987 ± 0.054	14.579 ± 0.036	Gaia DR2[b]
Parallax (mas)	4.438 ± 0.025	4.087 ± 0.021	Gaia DR2[b]
Epoch	2015.5	2015.5	Gaia DR2[b]
B (mag)	12.761 ± 0.015	13.326 ± 0.045	AAVSO DR9[c]
V (mag)	11.963 ± 0.069	12.039 ± 0.05	AAVSO DR9[c]
Gaia (mag)	11.7733 ± 0.00025	11.83746 ± 0.00023	Gaia DR2[b]
B_P (mag)	12.2037 ± 0.0017	12.82419 ± 0.00075	Gaia DR2[b]
R_P (mag)	11.21367 ± 0.00092	11.29765 ± 0.00055	Gaia DR2[b]
TESS (mag)	11.2595 ± 0.006	11.3458 ± 0.006	TIC V8[a]
J (mag)	10.616 ± 0.024	10.687 ± 0.026	2MASS[d]
H (mag)	10.207 ± 0.021	10.333 ± 0.022	2MASS[d]
K_S (mag)	10.108 ± 0.019	10.270 ± 0.023	2MASS[d]

Notes.
[a] Stassun et al. (2018b).
[b] Gaia Collaboration et al. (2018).
[c] Henden et al. (2016).
[d] Cutri et al. (2003).

2.1. TESS Photometry

TOI 694 (TIC 55383975; $V = 11.963$ mag) was observed by TESS Camera 4 during a total of 12 Sectors. It was observed in 2 minute cadence on Sector 1 (UT 2018 July 25–UT 2018 August 22), Sectors 4 through 9 (UT 2018 October 18–UT 2019 March 26), and Sectors 11 through 13 (UT 2019 April 22–UT 2019 July 18). The target was within the field of view also in Sectors 2 and 3 (UT 2018 August 22–UT 2018 October 18), but since it was not included in the pixel stamps observed with 2 minute exposures during those sectors we use the Full Frame Image (FFI) observations with a cadence of 30 minutes. TESS observations were interrupted between each of the 13.7 day long orbits of the satellite when data were downloaded to Earth. The 2 minute data were processed by the Science Processing Operations Center (SPOC; Jenkins et al. 2016) pipeline which produced two light curves per sector called Simple Aperture Photometry and Presearch Data Conditioning Simple Aperture Photometry (Smith et al. 2012; Stumpe et al. 2012, 2014) and identified 1.5% deep transit-like dips every 48.1 days. The FFIs were processed by the Quick Look Pipeline (QLP; C. X. Huang et al. 2020, in preparation). The TESS light curves are shown in Figures 1 and 2.

TIC 220568520 ($V = 12.039$ mag) was observed by TESS Camera 3 during Sectors 1 through 3, from UT 2018 July 25 to UT 2018 October 18. The target's light curve was derived from the FFIs, with a 30 minute exposure time, by QLP where transits were identified with a high signal-to-noise ratio (S/N) every 18.2 days. The TESS light curves are shown in Figures 3 and 4. The decreased scatter in Figures 3 and 4 relative to Figures 1 and 2 is due to the longer integration time, which decreases the noise per exposure.

2.2. Spectroscopic follow-up

To characterize the stellar properties of the primary star and measure the mass of the transiting companion we obtained series of spectroscopic observations with the 1.5 m SMARTS/CHIRON, ANU 2.3 m/Echelle, Euler 1.2 m/CORALIE, and MPG/ESO 2.2 m/FEROS facilities. The radial velocity (RV) measurements are summarized in Table 2 and shown in Figures 5 and 6 for TOI 694 and TIC 220568520, respectively.

For both objects we obtained time series RVs with the 1.5 m SMARTS/CHIRON facility (Tokovinin et al. 2013), located at Cerro Tololo Inter-American Observatory, Chile. The spectra were obtained with CHIRON in the fiber mode, with a spectral resolving power of $R \sim 25{,}000$ over the wavelength region 4100–8700 Å. These observations were used to constrain the systems' RV orbit. A total of 14 CHIRON spectra were obtained for TOI 694 from UT 2019 October 7 to UT 2020 February 17, and 10 spectra were obtained for TIC 220568520 from 2019 August 31 to 2019 October 7. RVs were measured from each spectrum by modeling their rotational line profiles, derived via a least-squares deconvolution (Donati et al. 1997) of the observed spectrum against a non-rotating synthetic

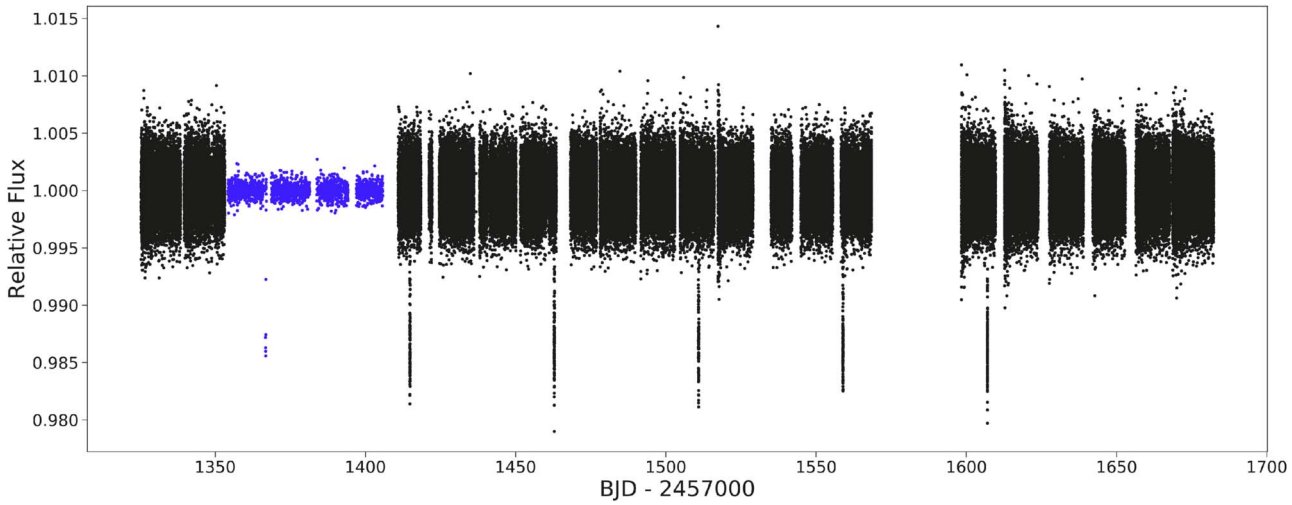

Figure 1. Detrended Science Processing Operations Center 2 minute (black) and Quick Look Pipeline 30 minute cadence (blue) TESS light curve of TOI 694. Six transits are clearly seen, five of which were observed with 2 minute cadences.

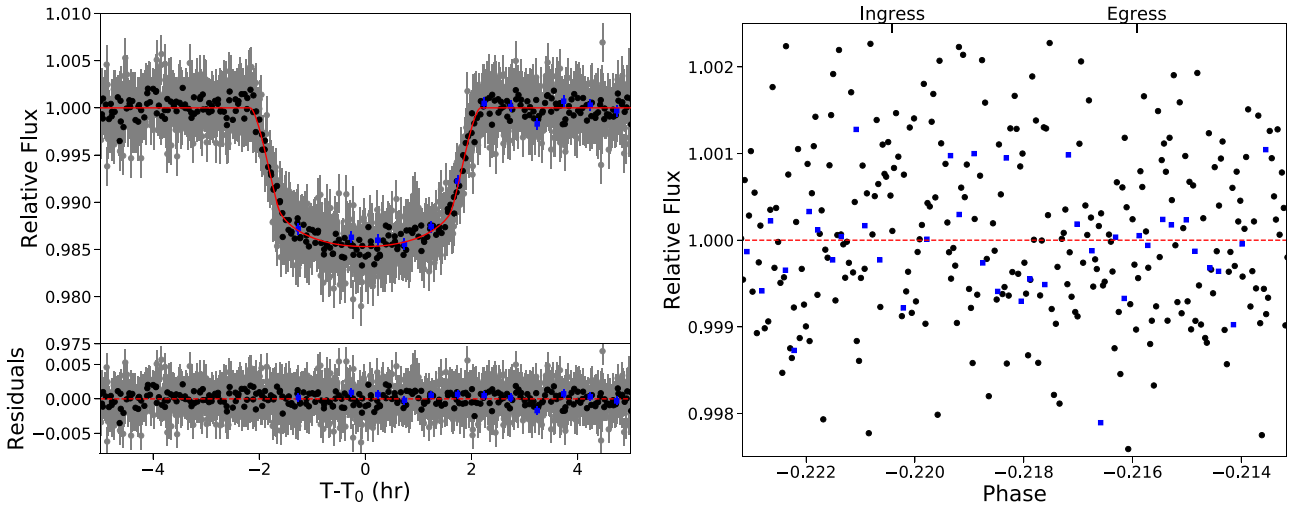

Figure 2. Zoom-in view of the phased TESS 2 minute cadence (gray), binned 2 minute cadence (black), and 30 minute cadence (blue) light curve of the TOI 694 transit (left panel) and secondary eclipse (right panel). In the left panel, the red line is the fitted transit model, and the residuals (data–model) are shown at the bottom. In the right panel, the dashed red line is the median relative flux value out of transit. The error bars are not shown in order to improve visibility. The ingress and egress points are denoted at the top of the figure.

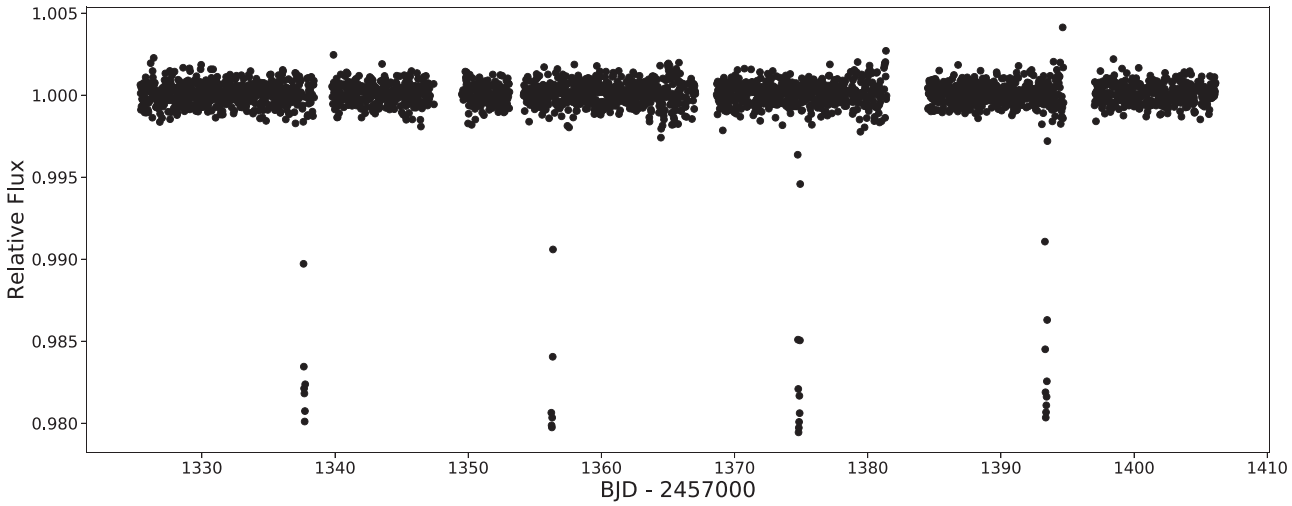

Figure 3. TESS light curve (30 minute cadence) of TIC 220568520 with four clear transit events.

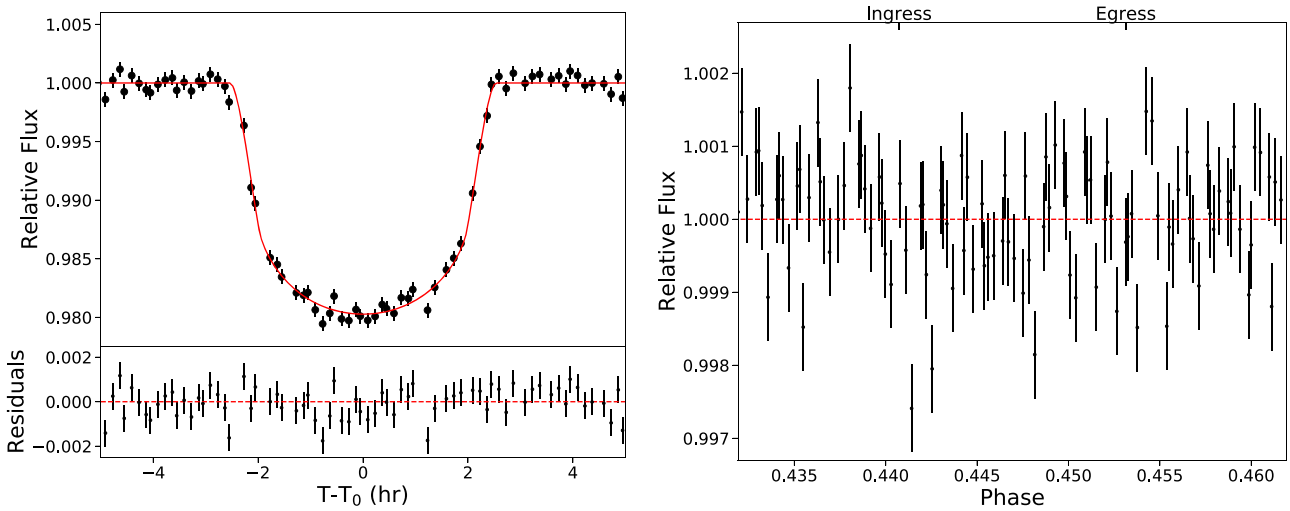

Figure 4. Zoom-in of the phased TESS light curve of TIC 220568520, centered on mid-transit (left) and the secondary eclipse (right). In the left panel, the red line is the fitted transit model, and the residuals (data–model) are shown at the bottom. In the right panel, the dashed red line is the median relative flux value out of transit.

template generated with the ATLAS-9 model atmospheres (Castelli & Hubrig 2004). The derived RVs are listed in Table 2. In addition, for each target a single CHIRON spectrum was observed in the slicer mode, with a resolving power of $R \sim 80{,}000$, to be used for spectral characterization of the primary star, described in Section 3.1.

For TIC 220568520 we measured RVs with the Australian National University (ANU) 2.3 m/Echelle spectrograph prior to obtaining the CHIRON spectra. The ANU 2.3 m/Echelle is a slit-fed medium-resolution spectrograph on the ANU 2.3 m telescope at Siding Spring Observatory (New South Wales, Australia). The spectrograph has a spectral resolving power of $\lambda/\Delta\lambda \equiv R \sim 23{,}000$ over the wavelength range 3900–6700 Å. A total of 11 spectra were obtained for TIC 220568520 with the ANU 2.3 m from UT 2019 January 17 to UT 2019 March 4, at an average S/N of ∼50 per resolution element over the Mg b triplet wavelength region for each observation. The spectra were reduced and extracted based on the procedure described in Zhou et al. (2014b), and are listed in Table 2.

We obtained nine observations of TOI-694 with the high-resolution spectrograph CORALIE on the Swiss 1.2 m Euler telescope at La Silla Observatory, Chile (Queloz et al. 2001) between UT 2019 October 17 and UT 2020 January 7. CORALIE has a resolution of $R \sim 60{,}000$ and is fed by two fibers: a 2″ on-sky science fiber encompassing the star and another fiber that can either connect to a Fabry–Pérot etalon for simultaneous wavelength calibration or on-sky for background subtraction of sky flux. We observed TOI-694 in the simultaneous Fabry–Pérot wavelength calibration mode using an exposure time of 1800 s. The spectra were reduced with the CORALIE standard reduction pipeline and RVs were computed for each epoch by cross-correlating with a binary G2 mask (Pepe et al. 2002).

TOI-694 was observed also with the Fiber-fed, Extended Range, Echelle Spectrograph (FEROS; Kaufer et al. 1999), mounted on the MPG/ESO 2.2 m telescope at La Silla, Chile. Observations were made by the WINE collaboration, which is focused on the systematic characterization of warm giant planets with TESS (Brahm et al. 2019; Jordán et al. 2020). Four spectra of TOI-694 were obtained between UT 2019 February 28 and UT 2019 March 17 with an exposure time of 900 s and an S/N ranging from 53 to 76. Observations were performed with the simultaneous calibration technique, where a comparison fiber was used to trace the instrumental variations during the science exposure by registering the spectrum of a ThAr lamp. FEROS data were reduced and processed with the `CERES` pipeline (Brahm et al. 2017) which uses the optimal extraction routines presented by Marsh (1989) and delivers precise RVs and bisector span measurements, presented in Table 2.

2.3. High Angular Resolution Imaging with SOAR HRCam

We used high angular resolution imaging to look for stars close to the targets' positions, within an angular separation of 1″–2″, which cannot be identified with regular seeing-limited imaging. If they exist, the small separation might prevent them from being detected by Gaia and included in the TESS Input Catalog, or TIC (Stassun et al. 2018b), leading to an inaccurate estimate of the extent by which light from the target is blended with light from nearby stars, leading in turn to a biased estimate of the intrinsic transit depth. It is also possible that nearby stars are the source of the variability seen in TESS data.

We observed both targets with the high-resolution camera (HRCam, Tokovinin 2018) mounted on the Southern Astrophysical Research (SOAR) 4.1 m telescope, in Cerro Pachón, Chile. HRCam uses the speckle interferometry technique in a visible bandpass similar to that of TESS. A detailed description of HRCam observations of TESS targets is available in Ziegler et al. (2020). We observed TOI 694 on UT 2019 July 14 and TIC 220568520 on UT 2019 November 9. For both targets we detected no nearby sources down to $\Delta\mathrm{mag} \approx 4.5$ mag at 0.″3 and $\Delta\mathrm{mag} \approx 5.0$ at 1.″0. The 5σ SOAR/HRCam detection sensitivity and the speckle autocorrelation function are plotted in Figures 7 and 8.

3. Data Analysis

3.1. Primary Star Parameters

3.1.1. MESA Isochrones and Stellar Tracks Analysis

For the primary star in each system we derived initial values of the spectral parameters, $T_{\rm eff}$, $\log g$, and $V \sin(I)$, by matching

Table 2
Radial Velocities

Time BJD	RV[a] km s^{-1}	Error km s^{-1}	Instrument
TOI 694[b]			
2458542.63751	21.4803	0.0076	FEROS
2458545.58904	22.5943	0.0071	FEROS
2458556.62596	28.8646	0.0095	FEROS
2458559.60797	23.0099	0.0077	FEROS
2458763.86992	16.2069	0.0149	CHIRON
2458772.79219	17.0740	0.0104	CHIRON
2458773.77718	17.1886	0.0145	CHIRON
2458783.80427	19.5069	0.0068	CHIRON
2458789.75347	22.5803	0.0252	CHIRON
2458798.66760	23.0389	0.0159	CHIRON
2458803.64710	17.3233	0.0147	CHIRON
2458808.77574	16.2327	0.0156	CHIRON
2458873.59450	17.9937	0.0422	CHIRON
2458884.55191	21.6734	0.0214	CHIRON
2458889.56772	25.8525	0.0477	CHIRON
2458891.61208	27.4781	0.0359	CHIRON
2458893.56327	25.6463	0.0351	CHIRON
2458896.53063	19.8216	0.0386	CHIRON
2458773.75679	19.5107	0.0396	CORALIE
2458777.80659	20.2075	0.0631	CORALIE
2458781.77898	21.1769	0.0293	CORALIE
2458783.78105	21.8304	0.0406	CORALIE
2458786.77769	23.0417	0.0366	CORALIE
2458821.69504	19.4387	0.0295	CORALIE
2458842.72232	29.3174	0.0362	CORALIE
2458847.67201	23.4254	0.0283	CORALIE
2458855.64763	18.7321	0.0783	CORALIE
TIC 220568520[c]			
2458500.97894	30.5575	0.0318	ANU 2.3 m/Echelle
2458502.09007	29.4386	0.5716	ANU 2.3 m/Echelle
2458505.04661	21.8699	0.0795	ANU 2.3 m/Echelle
2458506.00173	20.9493	0.2224	ANU 2.3 m/Echelle
2458532.91371	27.4253	0.2931	ANU 2.3 m/Echelle
2458534.91425	30.0442	0.1773	ANU 2.3 m/Echelle
2458536.92492	30.8171	0.1309	ANU 2.3 m/Echelle
2458537.91918	31.2864	0.2634	ANU 2.3 m/Echelle
2458538.90685	30.8376	0.1639	ANU 2.3 m/Echelle
2458541.95366	22.7282	0.3439	ANU 2.3 m/Echelle
2458546.92590	18.4931	0.3579	ANU 2.3 m/Echelle
2458726.90477	24.0542	0.0239	CHIRON
2458730.83770	15.3734	0.0217	CHIRON
2458740.84783	29.9363	0.0211	CHIRON
2458747.84631	17.6927	0.0115	CHIRON
2458749.85537	15.2544	0.0140	CHIRON
2458751.80097	17.1443	0.0172	CHIRON
2458753.79406	21.5104	0.0119	CHIRON
2458757.80128	29.1168	0.0187	CHIRON
2458761.75638	28.8378	0.0263	CHIRON
2458763.82222	24.6238	0.0131	CHIRON

Notes.
[a] All RVs are barycentric.
[b] The Gaia DR2 RV is 20.70 ± 2.22 km s^{-1} (Lindegren et al. 2018).
[c] The Gaia DR2 RV is 28.09 ± 1.79 km s^{-1} (Lindegren et al. 2018).

each CHIRON spectrum against a library of ∼10,000 observed spectra classified by the Stellar Parameter Classification routine (Buchhave et al. 2012).

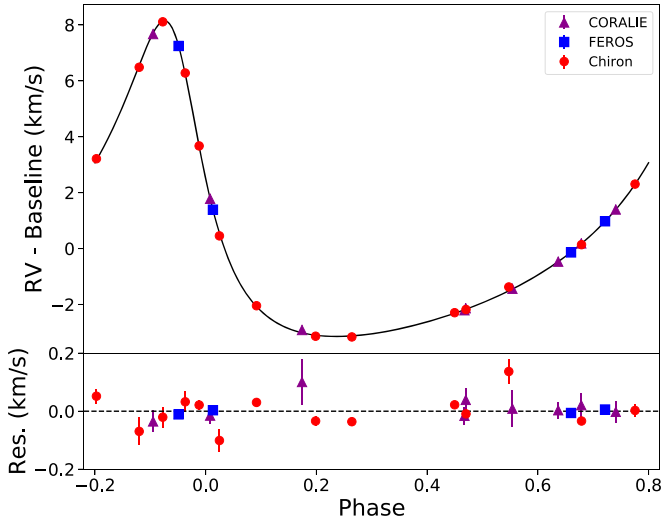

Figure 5. Radial velocity curve of TOI 694 phase folded to the orbital period of the companion. The different colors and markers correspond to the different instruments used to obtain the data, and the black line denotes the best-fit model. The residuals for each instrument are shown in the bottom panel.

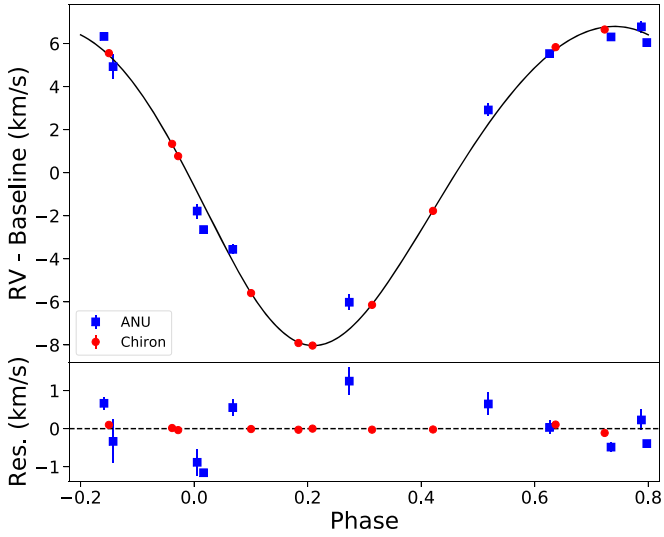

Figure 6. Radial velocity curve of TIC 220568520 phase folded to the orbital period of the companion. The different colors and markers correspond to the different instruments used to obtain the data, and the black line denotes the best-fit model. The residuals for each instrument are shown in the bottom panel.

We then used the spectroscopic parameters along with the Gaia DR2 parallax and magnitudes (G, B_P, R_P), 2MASS magnitudes (J, H, K_S), and AAVSO magnitudes (B, V) to perform an isochrone fit in order to further constrain the spectroscopic parameters and derive physical parameters for the primary stars. The spectroscopic parameters, parallax, and magnitudes are used as priors to determine the goodness of fit. We used the *isochrone* package (Morton 2015) to generate the isochrone models used to sample the stellar parameters and found the best-fit parameters using a Markov chain Monte Carlo (MCMC) routine. The routine consisted of 40 independent walkers each taking 25,000 steps, of which the first 2000 were discarded as burn-in.

The fitted spectroscopic parameters and derived physical parameters for the primary stars in each of the two systems

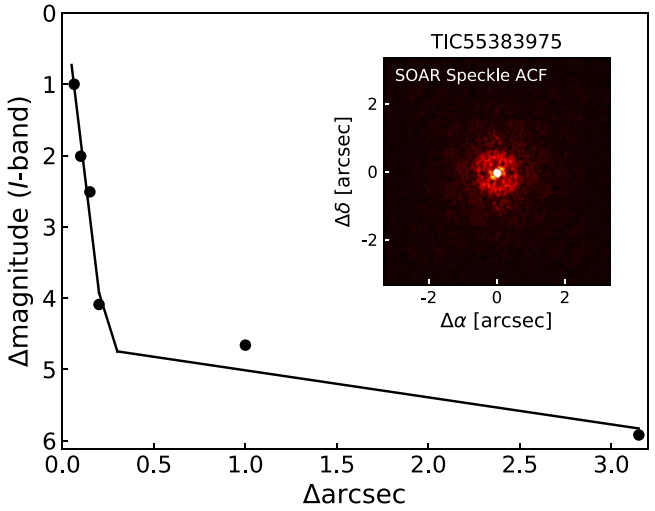

Figure 7. Contrast curves showing the 5σ detection sensitivity and speckle autocorrelation functions obtained in the *I*-band using SOAR/HRCam for TOI 694 (TIC 55383975).

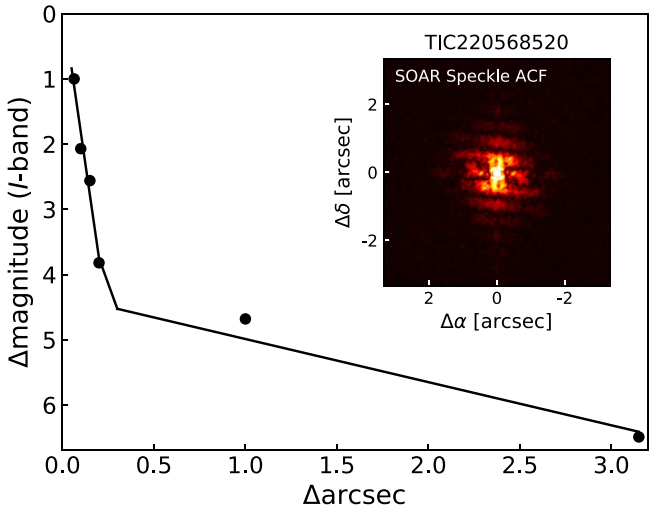

Figure 8. Contrast curves showing the 5σ detection sensitivity and speckle autocorrelation functions obtained in the *I*-band using SOAR/HRCam for TIC 220568520.

studied here are reported in Table 3. Both primary stars are similar to each other, and similar to the Sun (within 1–2σ) albeit with higher metallicities.

3.1.2. Spectral Energy Distribution Analysis

For both TOI 694 and TIC 220568520 we performed an analysis of the broadband spectral energy distribution (SED) together with the Gaia DR2 parallax in order to determine an empirical measurement of the stellar radius, following the procedures described in Stassun & Torres (2016) and Stassun et al. (2017, 2018a). We pulled the *BV gri* magnitudes from APASS, the JHK_S magnitudes from 2MASS, the W1–W4 magnitudes from the Wide-field Infrared Survey Explorer, and the $GG_{\rm BP}G_{\rm RP}$ magnitudes from Gaia. We also considered the Galaxy Evolution Explorer NUV flux for evidence of chromospheric activity. Together, the available photometry spans the full stellar SED over the wavelength range 0.2–22 μm (see Figure 9).

Table 3
Fitted and Derived Parameters

Parameter	TOI 694		TIC 220568520	
	Value	Error	Value	Error
Host star parameters				
M_1 ($M_\odot$)	0.967	$^{+0.047}_{-0.040}$	1.030	$^{+0.043}_{-0.042}$
R_1 ($R_\odot$)	0.998	$^{+0.010}_{-0.012}$	1.007	$^{+0.010}_{-0.009}$
ρ_1[a] (g cm^{-3})	1.51	$^{+0.15}_{-0.13}$	1.445	$^{+0.064}_{-0.074}$
L_1 ($L_\odot$)	0.819	$^{+0.047}_{-0.044}$	0.890	$^{+0.047}_{-0.044}$
$T_{\rm eff}$ (K)	5496	$^{+87}_{-81}$	5589	81
[Fe/H]	0.21	0.08	0.26	0.07
log g	4.425	$^{+0.028}_{-0.025}$	4.445	$^{+0.023}_{-0.025}$
Age(Gyr)	7.33	$^{+2.92}_{-3.02}$	4.09	$^{+2.60}_{-2.28}$
$V \sin(I)$ (km s^{-1})	2.18	0.5	3.4	0.5
Fitted parameters				
$q_{1,\rm TESS}$	0.345	$^{+0.078}_{-0.070}$	0.418	$^{+0.080}_{-0.074}$
$q_{2,\rm TESS}$	0.308	$^{+0.084}_{-0.079}$	0.374	0.071
R_2/R_1	0.1145	$^{+0.0012}_{-0.0013}$	0.1274	$^{+0.0014}_{-0.0013}$
$(R_1 + R_2)/a$	0.01960	0.00064	0.03791	$^{+0.00070}_{-0.00056}$
cos i	0.0152	$^{+0.0020}_{-0.0023}$	0.0075	$^{+0.0030}_{-0.0040}$
T_0 (BJD—2,457,000)	1366.77176	0.00064	1337.72060	0.00082
P (d)	48.05131	0.00019	18.55769	0.00039
K (km s^{-1})	5.645	0.011	7.428	0.035
$\sqrt{e}\cos\omega$	0.61438	$^{+0.00072}_{-0.00078}$	−0.2709	0.0080
$\sqrt{e}\sin\omega$	0.3768	$^{+0.0016}_{-0.0015}$	0.151	0.016
$\gamma_{c,\rm ANU}$ (km s^{-1})	⋯	⋯	24.50	0.22
$\gamma_{c,\rm CHIRON}$ (km s^{-1})	19.368	0.013	23.285	0.028
$\gamma_{c,\rm FEROS}$ (km s^{-1})	21.6187	0.0062	⋯	⋯
$\gamma_{c,\rm CORALIE}$ (km s^{-1})	21.645	0.012	⋯	⋯
ln $\sigma_{c,\rm ANU}$ (km s^{-1})	⋯	⋯	−0.37	$^{+0.21}_{-0.23}$
ln $\sigma_{c,\rm CHIRON}$ (km s^{-1})	−3.21	0.34	−2.56	$^{+0.36}_{-0.30}$
ln $\sigma_{c,\rm FEROS}$ (km s^{-1})	−12.7	6.9	⋯	⋯
ln $\sigma_{c,\rm CORALIE}$ (km s^{-1})	−13.5	6.5	⋯	⋯
ln $\sigma_{c,\rm TESS_{SC}}$[b]	−6.242	0.012	⋯	⋯
ln $\sigma_{c,\rm TESS_{LC}}$[c]	−7.21	$^{+0.20}_{-0.17}$	−7.313	0.055
Derived parameters				
i ($^\circ$)	89.13	$^{+0.13}_{-0.11}$	89.57	$^{+0.23}_{-0.17}$
a(au)	0.2638	$^{+0.0092}_{-0.0086}$	0.1391	$^{+0.0025}_{-0.0027}$
b[d]	0.497	$^{+0.048}_{-0.060}$	0.211	$^{+0.081}_{-0.11}$
$T_{\rm tot}$[e] (hr)	4.328	$^{+0.037}_{-0.035}$	5.018	0.035
$T_{\rm full}$[f] (hr)	3.179	0.068	3.834	$^{+0.050}_{-0.058}$
e	0.51946	0.00081	0.0964	$^{+0.0034}_{-0.0030}$
ω (deg)	31.52	$^{+0.13}_{-0.12}$	150.9	3.2
R_2 ($R_{\rm Jup}$)	1.111	0.017	1.248	0.018
M_2 ($M_{\rm Jup}$)	89.0	5.3	107.2	5.2

Notes.
[a] Derived from simultaneous fit of TESS photometry and RV measurements.
[b] TESS 2 minute cadence data.
[c] TESS 30 minute cadence data.
[d] Impact parameter.
[e] From first to last (fourth) contacts.
[f] From second to third contacts.

We performed a fit using Kurucz stellar atmosphere models, with the priors on effective temperature ($T_{\rm eff}$), surface gravity (log g), and metallicity ([Fe/H]) from the analysis of the CHIRON spectra. The remaining free parameter is the extinction (A_V), which we limited to the maximum permitted for the star's line of sight from the Schlegel et al. (1998) dust maps. The resulting fits, plotted

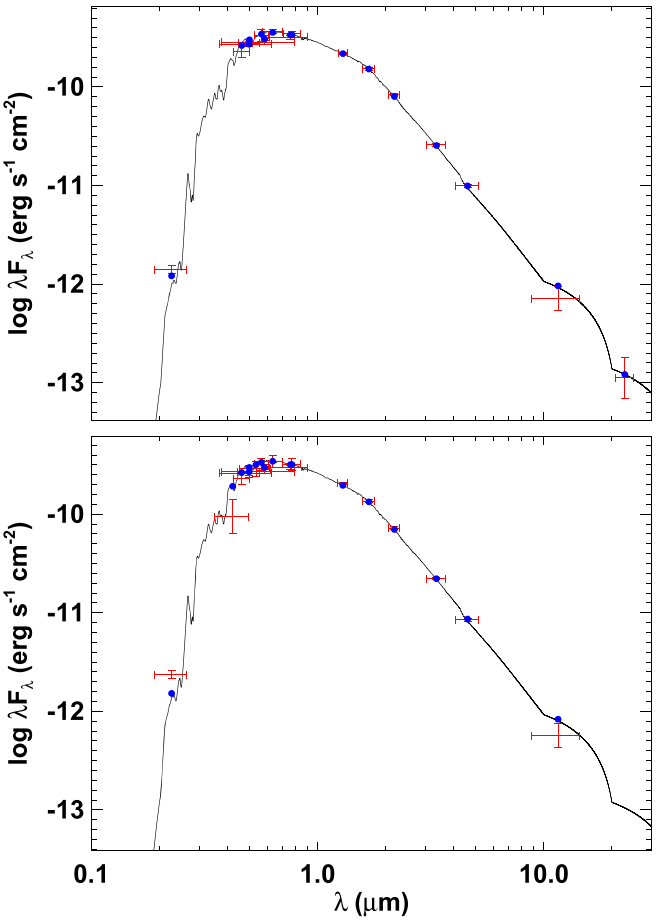

Figure 9. Spectral energy distribution for TOI 694 (top) and TIC 220568520 (bottom). Red symbols represent the observed photometric measurements, where the horizontal bars represent the effective width of the passband. Blue symbols are the model fluxes from the best-fit Kurucz atmosphere model (black).

in Figure 9, have a reduced χ^2 of 1.3 and 2.1, and $A_V = 0.12 \pm 0.02$ and 0.06 ± 0.02, for TOI 694 and TIC 220568520, respectively. Integrating the model SED gives the bolometric flux at Earth of $F_{\rm bol} = 5.199 \pm 0.060 \times 10^{-10}$ erg s^{-1} cm^{-2} and $4.77 \pm 0.11 \times 10^{-10}$ erg s^{-1} cm^{-2}, respectively. Taking $F_{\rm bol}$ and $T_{\rm eff}$ together with the Gaia parallax, adjusted by $+0.08$ mas to account for the systematic offset reported by Stassun & Torres (2018), gives the stellar radii as $R_s = 0.992 \pm 0.037$ $R_\odot$ and 0.992 ± 0.038 $R_\odot$, respectively.

3.1.3. Stellar Mass via Radius and Surface Gravity

The empirical stellar radii determined above also affords an opportunity to estimate the stellar masses empirically, via the spectroscopically determined surface gravity ($\log g = 4.45 \pm 0.10$ and 4.34 ± 0.10, respectively). For TOI 694 and TIC 220568520 we obtain $M_s = 1.01 \pm 0.13$ $M_\odot$ and 0.79 ± 0.19 $M_\odot$, respectively. These are similar to the values estimated via the eclipsing-binary-based relations of Torres et al. (2010), which give $M_s = 1.00 \pm 0.06$ $M_\odot$ and 1.09 ± 0.07 $M_\odot$, respectively. For TOI 694, these values are nearly identical. For TIC 220568520, they differ by less than 2σ.

3.1.4. Stellar Age via Gyrochronology

We estimate each star's age from its rotational period, $P_{\rm rot}$, which we calculate from the spectroscopic $V \sin(I)$ together with the empirically determined radius above, assuming $I = 90°$. For TOI 694 and TIC 220568520 we obtain $P_{\rm rot} \approx 24.1 \pm 5.6$ d and 15.5 ± 2.3 d, respectively. From the rotation–activity–age relations of Mamajek & Hillenbrand (2008), we obtain from the $P_{\rm rot}$ and the stellar $B - V$ colors ages of $\tau = 3.8 \pm 0.4$ Gyr and 2.3 ± 0.3 Gyr, respectively.

3.2. Simultaneous Transit and RV Fit

In order to derive the orbital parameters and companion's radius and mass, we performed model fitting using ALLESFITTER[24] (Günther & Daylan 2019, 2020), enabling a joint analysis of the TESS transit light curve and the RV orbit. ALLESFITTER is publicly available, and provides an environment to analyze light curves and RVs of binary star and star–planet systems. It is based on various public packages including ELLC for light curve and RV modeling (Maxted 2016) and EMCEE for MCMC sampling (Foreman-Mackey et al. 2013).

We fit the following parameters.

1. Quadratic stellar limb-darkening parameters q_1 and q_2, using the transformation from Kipping (2013), with Gaussian priors centered on values derived from Claret (2017). We chose the Gaussian prior width (1σ) to be 0.1, which reflects the uncertainties on the host stars parameters.
2. Radius ratio, R_2/R_1, where 1 denotes the primary star and 2 the secondary, with uniform prior from 0 to 1.
3. Sum of radii divided by the orbital semimajor axis, $(R_1 + R_2)/a$, with uniform prior from 0 to 1.
4. Cosine of the orbital inclination, $\cos i$, with uniform prior from 0 to 1.
5. Orbital period, P with uniform prior from 0 to 10^{12} days.
6. Primary eclipse epoch, T_0, with uniform prior from 0 to 10^{12} days.
7. RV semi-amplitude, K, with uniform prior from 0 to 50 km s^{-1}.
8. Eccentricity parameters $\sqrt{e}\cos\omega$ and $\sqrt{e}\sin\omega$, each with uniform prior from -1 to 1, where e is the orbital eccentricity and ω the argument of periastron.
9. RV zero-point, γ_c, for each of the RV data sets.
10. RV jitter terms, σ_c, for each of the RV data sets.
11. White noise scaling term for the TESS data, $\sigma_{c,\rm TESS}$.

Initial guesses for the values of q_1 and q_2 were obtained by matching the spectroscopic parameters of each primary star to the closest values of the coefficients u_1 and u_2 of the quadratic limb-darkening law listed in Claret (2017), and transforming them to the corresponding values of q_1 and q_2. Initial guesses for R_2/R_1, $(R_1 + R_2)/a$, $\cos i$, P, and T_0 were obtained using values provided by the SPOC Data Validation Report for TOI 694 (Li et al. 2019) and the QLP Data Validation Report for TIC 220568520. Initial guesses for K and the 4 γ_c terms were obtained by visually inspecting each data set. We used an MCMC algorithm to explore the parameter space and determine the best-fit parameters. We initialized the MCMC with 100 walkers, performing two preliminary runs of 1000 steps per walker to obtain higher-likelihood initial guesses for the nominal run of 15,000 steps per walker. We then discarded the first 2000 steps for each chain as burn-in phase before thinning the chains by a factor of 10 and calculating the final posterior distributions. The values and errors of the fitted and derived parameters listed in

[24] https://github.com/MNGuenther/allesfitter

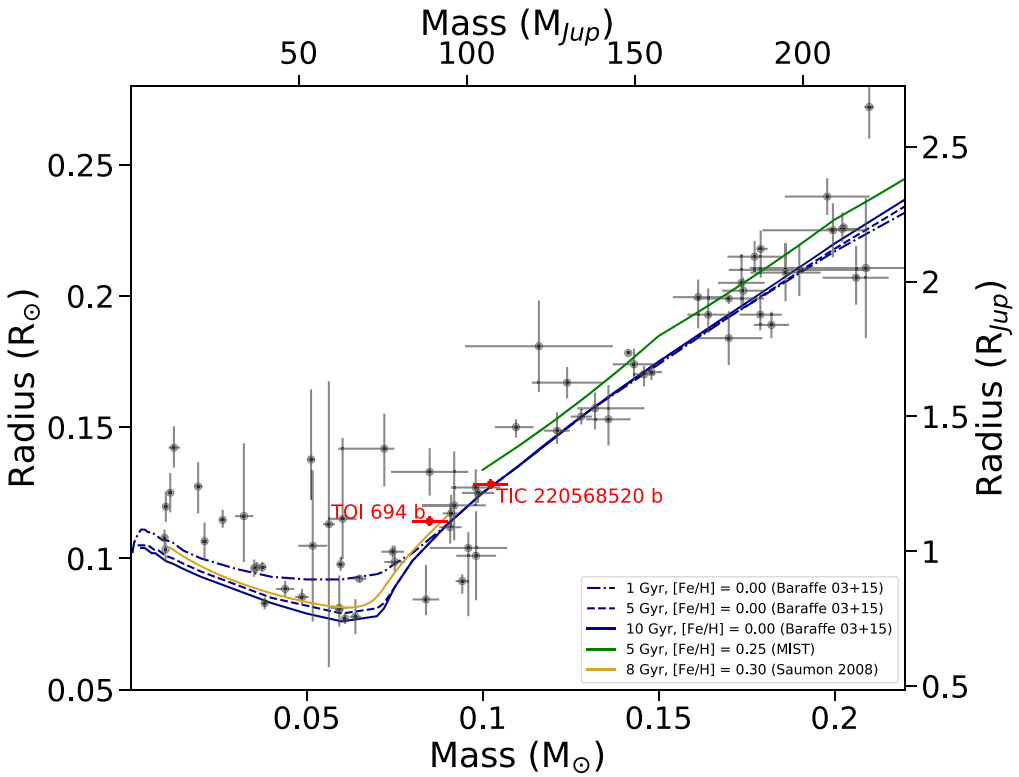

Figure 10. Radius–mass diagram for the massive planets, brown dwarfs, and low-mass stars listed in Table 4. The blue lines are models for low-mass stars and substellar objects with solar metallicity from Baraffe et al. (2003, 2015). The green line is derived from MESA isochrones and stellar tracks for [Fe/H] = 0.25. The gold line is a model from Saumon & Marley (2008) for [Fe/H] = 0.3. RIK 72 b is a ~60 $M_{\rm Jup}$ transiting brown dwarf that is not shown due to its inflated radius of 3.10 $R_{\rm Jup}$ (David et al. 2019).

Table 3 are defined as the median values and 68% confidence intervals of the posterior distributions, respectively. The best-fit transit model light curve and RV model curve for TOI 694 are shown in Figures 2 and 5, respectively. For TIC 220568520, they are shown in Figures 4 and 6.

4. Discussion

From the simultaneous fits of the TESS transit photometry and RV data, we derive the TOI 694 b mass and radius to be 89.0 ± 5.3 $M_{\rm Jup}$ (0.0849 ± 0.0051 $M_\odot$) and 1.111 ± 0.017 $R_{\rm Jup}$ (0.1142 ± 0.0017 $R_\odot$), respectively, and the TIC 220568520 b mass and radius to be 107.2 ± 5.2 $M_{\rm Jup}$ (0.1023 ± 0.0050 $M_\odot$) and 1.248 ± 0.018 $R_{\rm Jup}$ (0.1282 ± 0.0019 $R_\odot$), respectively. We note that mass uncertainties are dominated by the primary star mass uncertainties and not the orbital parameter uncertainties.

The two binary companions measured here are among the smallest stars with a measured radius and mass. To show them in the context of similar objects we plot in Figure 10 the radius–mass diagram spanning brown dwarfs and small stars, with a mass range of 0.01–0.21 $M_\odot$. We mark on that diagram the new objects studied here (in red), and objects within that mass range that have a measured radius reported in the literature which we list in Table 4,[25] with the exception of the inflated brown dwarf RIK 72 b (David et al. 2019).

We also plot in the radius–mass diagram the theoretical isochrones for solar metallicity at ages of 1, 5, and 10 Gyr taken from Baraffe et al. (2003, 2015), and the MESA isochrones and stellar tracks (MIST[26]; Paxton et al. 2011, 2013; Dotter 2016; Choi et al. 2016) at 5 Gyr with solar metallicity and metallicity of [Fe/H] = 0.25. The latter is close to the metallicity we measure for the primary star in TIC 220568520 which we assume is also the metallicity of the secondary.

The position in the radius–mass diagram of TOI 694 studied here is consistent with the 8 Gyr and [Fe/H] = 0.30 isochrone from Saumon & Marley (2008). In contrast, the position of TIC 220568520 is slightly *below* the MIST relation for [Fe/H] = 0.25, with a distance in radius of about 5%. This small inconsistency is in the opposite direction of the inflated radius identified for stars of similar mass (e.g., Ribas 2006; Torres et al. 2010; Burrows et al. 2011; Kesseli et al. 2018) and is believed to be the result of enhanced magnetic fields in rapidly rotating stars (e.g., Chabrier et al. 2007). However, the recent work of Han et al. (2019) and von Boetticher et al. (2019) showed that the radii of many low-mass fully convective stars are consistent with theoretical expectations without invoking enhanced magnetic fields.

Fast rotation, which leads to enhanced magnetic fields, can result from spin–orbit tidal synchronization of short-period systems (Mazeh 2008). The two systems studied here have relatively long orbital periods, of 18.6 days (TIC 220568520) and 48.1 days (TOI 694), longer than 95% (TOI 694) and 87% (TIC 220568520) of the systems listed in Table 4. Therefore these systems are not expected to have reached tidal synchronization. Even if the low-mass binary companions have reached pseudo-synchronization

[25] The list given in Table 4 is the result of our efforts to compile all objects reported in the literature within the mass range of 0.01–0.21 $M_\odot$ whose radius is also measured. While we recognize the possibility that a few objects may have unintentionally been omitted from such a compilation, such omission is highly unlikely to change the characaristics of the population of these objects, as presented in Figure 10 and 11 and discussed in the text.

[26] http://waps.cfa.harvard.edu/MIST/

Table 4
Catalog of Low-mass Companions with Measured Masses and Radii

System	M_2 (M_J)	σ_{M_2} (M_J)	R_2 (R_J)	σ_{R_2} (R_J)	P (days)	e	σ_e	M_1 ($M_\odot$)	σ_{M_1} ($M_\odot$)	R_1 ($R_\odot$)	σ_{R_1} ($R_\odot$)	$T_{\rm eff}$ (K)	$\sigma_{T_{\rm eff}}$ (K)	Reference
Kepler-75	10.1	0.4	1.05	0.03	8.88	0.57	0.01	0.91	0.04	0.89	0.02	5200	100	Bonomo et al. (2015)
CoRoT-27	10.4	0.6	1.01	0.04	3.57	0[a]	⋯	1.05	0.11	1.08	$^{+0.16}_{-0.08}$	5900	120	Parviainen et al. (2014)
WASP-18	10.52	0.38	1.165	0.057	0.94	0.0092	0.0028	1.281	0.069	1.230	0.047	6400	100	Southworth et al. (2009)
XO-3	11.8	0.6	1.22	0.07	3.19	0.260	0.017	1.21	0.07	1.38	0.08	6429	100	Winn et al. (2008)
HATS 70	12.9	$^{+1.8}_{-1.6}$	1.384	$^{+0.079}_{-0.074}$	1.888	<0.18	⋯	1.78	0.12	1.881	$^{+0.059}_{-0.066}$	7930	$^{+630}_{-820}$	Zhou et al. (2019)
Kepler-39	20.1	$^{+1.3}_{-1.2}$	1.24	$^{+0.09}_{-0.10}$	21.09	0.112	0.057	1.29	$^{+0.06}_{-0.07}$	1.40	0.10	6350	100	Bonomo et al. (2015)
CoRoT-3	22.0	0.7	1.037	0.069	4.26	0[a]	⋯	1.37	0.09	1.56	0.09	6740	140	Deleuil et al. (2008)
KELT-1	27.38	0.93	1.116	$^{+0.038}_{-0.029}$	1.22	0.01	$^{+0.010}_{-0.007}$	1.335	0.063	1.471	$^{+0.045}_{-0.035}$	6516	49	Siverd et al. (2012)
NLTT 41135	33.7	$^{+2.8}_{-2.6}$	1.13	$^{+0.27}_{-0.17}$	2.889	0[a]	⋯	0.188	$^{+0.026}_{-0.022}$	0.21	$^{+0.016}_{-0.014}$	3230	130	Irwin et al. (2010)
EPIC 219388192	36.8	1.0	0.937	0.032	5.29	0.1929	0.0019	1.01	0.04	1.01	0.03	5850	85	Nowak et al. (2017)
WASP-128	37.5	0.8	0.94	0.02	2.21	0[a]	⋯	1.16	0.04	1.16	0.02	5950	50	Hodžić et al. (2018)
CWW 89 A	39.21	1.10	0.941	0.019	5.293	0.1891	0.0022	1.101	$^{+0.039}_{-0.045}$	1.029	0.016	5755	49	Carmichael et al. (2019)
KOI 205	39.9	1.0	0.807	0.022	11.72	<0.031	⋯	0.925	0.033	0.841	0.020	5237	60	Díaz et al. (2013)
TOI 1406	46.0	2.7	0.86	0.03	10.57415	0[a]	⋯	1.18	0.09	1.35	0.03	6290	100	Carmichael et al. (2020)
EPIC 212036875	51	2	0.83	0.03	5.17	0.134	0.002	1.15	0.08	1.41	0.05	6230	90	Persson et al. (2019)
TOI-503	53.7	1.2	1.34	$^{+0.26}_{-0.15}$	3.677	0[a]	⋯	1.80	0.06	1.70	0.05	7650	160	Šubjak et al. (2019)
AD 3116	54.2	4.3	1.02	0.28	1.983	0.146	$^{+0.024}_{-0.016}$	0.276	0.020	0.29	0.08	3184	29	Gillen et al. (2017)
CoRoT-33	59	$^{+1.8}_{-1.7}$	1.1	0.53	5.819	0.07	0.0016	0.86	0.04	0.94	$^{+0.14}_{-0.08}$	5225	80	Csizmadia et al. (2015)
RIK 72	59.2	6.8	3.10	0.31	97.76	0.146	0.0116	0.439	0.044	0.961	0.096	3349	142	David et al. (2019)
LHS 6343 C	62.1	1.2	0.783	0.011	12.713	0.03	0.002	0.358	0.011	0.373	0.005	3431	21	Montet et al. (2015)
KOI 415	62.1	2.7	0.790	$^{+0.120}_{-0.070}$	166.8	0.698	0.002	0.94	0.06	1.250	$^{+0.015}_{-0.010}$	5810	80	Moutou et al. (2013)
WASP-30	62.50	1.20	0.951	$^{+0.028}_{-0.024}$	4.16	<0.0044	⋯	1.249	$^{+0.032}_{-0.036}$	1.389	$^{+0.033}_{-0.025}$	6202	$^{+42}_{-51}$	Triaud et al. (2013)
CoRoT-15	63.1	4.1	1.12	$^{+0.30}_{-0.15}$	3.06	0[a]	⋯	1.32	0.12	1.46	$^{+0.31}_{-0.14}$	6350	200	Bouchy et al. (2011)
TOI 569	63.8	1.0	0.75	0.02	6.55604	0[a]	⋯	1.21	0.03	1.48	0.03	5705	76	Carmichael et al. (2020)
EPIC 201702477	66.9	1.7	0.757	0.065	40.74	0.2281	0.0026	0.870	0.031	0.901	0.057	5571	70	Bayliss et al. (2017)
LP 261-75	68.1	2.1	0.898	0.015	1.882	<0.007	⋯	0.300	0.015	0.313	0.005	3100	50	Irwin et al. (2018)
NGTS-7A	75.5	$^{+3}_{-13.7}$	1.38	$^{+0.13}_{-0.14}$	0.676	0[a]	⋯	0.480	0.075	0.61	0.06	3359	$^{+106}_{-89}$	Jackman et al. (2019)
KOI 189	78.0	3.4	0.998	0.023	30.36	0.2746	0.0037	0.764	0.051	0.733	0.017	4952	40	Díaz et al. (2014)
Kepler-503	78.6	3.1	0.96	$^{+0.06}_{-0.04}$	7.258	0.025	$^{+0.014}_{-0.012}$	1.154	$^{+0.047}_{-0.042}$	1.764	$^{+0.08}_{-0.068}$	5690	$^{+100}_{-110}$	Cañas et al. (2018)
EBLM J0555-57	87.90	3.98	0.821	$^{+0.128}_{-0.058}$	7.758	0.0895	$^{+0.0035}_{-0.0036}$	1.180	$^{+0.082}_{-0.079}$	1.00	$^{+0.14}_{-0.07}$	6386	124	von Boetticher et al. (2019)
OGLE-TR-123	89.0	11.5	1.294	0.088	1.8	0[a]	⋯	1.29	0.26	1.55	0.1	6700	300	Pont et al. (2006)
TOI 694	89.8	5.3	1.11	0.02	48.05125	0.5212	0.0021	0.967	$^{+0.047}_{-0.04}$	0.998	$^{+0.010}_{-0.012}$	5496	$^{+87}_{-81}$	This work
KOI-607	95.1	$^{+3.4}_{-3.3}$	1.089	$^{+0.089}_{-0.061}$	5.894	0.395	$^{+0.0091}_{-0.0090}$	0.993	$^{+0.050}_{-0.052}$	0.915	$^{+0.031}_{-0.028}$	5418	$^{+87}_{-85}$	Carmichael et al. (2019)
J1219-39	95.4	$^{+1.9}_{-2.5}$	1.140	$^{+0.069}_{-0.049}$	6.76	0.05539	$^{+0.00023}_{-0.00022}$	0.826	$^{+0.032}_{-0.029}$	0.811	$^{+0.038}_{-0.024}$	5412	$^{+81}_{-65}$	Triaud et al. (2013)
OGLE-TR-122	96.3	9.4	1.17	$^{+0.20}_{-0.13}$	7.27	0.205	0.008	0.98	0.14	1.05	$^{+0.20}_{-0.09}$	5700	300	Pont et al. (2005a)
K2-76	98.7	2.0	0.889	$^{+0.025}_{-0.047}$	11.99	0.2545	$^{+0.0070}_{-0.0065}$	0.964	0.026	1.171	$^{+0.033}_{-0.060}$	5747	$^{+64}_{-70}$	Shporer et al. (2017)
C101186644	101	12	1.01	$^{+0.06}_{-0.25}$	20.68	0.402	⋯	1.2	0.2	1.07	0.07	6090	200	Tal-Or et al. (2013)
J2343 + 29	103	7	1.236	0.068	16.95	0.161	$^{+0.0015}_{-0.0027}$	0.864	$^{+0.097}_{-0.098}$	0.854	$^{+0.050}_{-0.060}$	5150	$^{+90}_{-60}$	Chaturvedi et al. (2016)
EBLM J0954-23	102.8	$^{+6.0}_{-5.9}$	0.983	0.165	7.575	0.04186	$^{+0.00094}_{-0.00092}$	1.166	$^{+0.080}_{-0.082}$	1.23	0.17	6406	124	von Boetticher et al. (2019)
KOI 686	103	5	1.22	0.04	52.51	0.556	0.0037	0.983	0.074	1.04	0.03	5750	120	Díaz et al. (2014)
TIC 220568520	107.8	5.2	1.248	0.018	18.55741	0.0956	$^{+0.0032}_{-0.0030}$	1.030	$^{+0.043}_{-0.042}$	1.007	$^{+0.010}_{-0.009}$	5589	81	This work
HATS 550-016	115	$^{+5}_{-6}$	1.46	$^{+0.03}_{-0.04}$	2.05	0.08	−1	0.97	$^{+0.05}_{-0.06}$	1.22	$^{+0.02}_{-0.03}$	6420	90	Zhou et al. (2014a)
OGLE-TR-106	121	22	1.76	0.17	2.54	0	0.02	⋯	⋯	1.31	0.09	⋯	⋯	Pont et al. (2005b)
EBLM J1431-11	126.9	$^{+3.77}_{-3.87}$	1.447	$^{+0.0681}_{-0.0487}$	4.45	0[a]	⋯	1.200	$^{+0.056}_{-0.055}$	1.114	$^{+0.043}_{-0.028}$	6161	124	von Boetticher et al. (2019)

Table 4
(Continued)

System	M_2 (M_J)	σ_{M_2} (M_J)	R_2 (R_J)	σ_{R_2} (R_J)	P (days)	e	σ_e	M_1 ($M_\odot$)	σ_{M_1} ($M_\odot$)	R_1 ($R_\odot$)	σ_{R_1} ($R_\odot$)	$T_{\rm eff}$ (K)	$\sigma_{T_{\rm eff}}$ (K)	Reference
HAT-TR-205-013	130	11	1.63	0.06	2.23	0.012	0.021	1.04	0.13	1.28	0.04	6295	⋯	Beatty et al. (2007)
TIC 231005575	134.1	3.1	1.499	0.029	61.777	0.298	$^{+0.004}_{-0.001}$	1.045	0.035	0.992	0.050	5500	85	Gill et al. (2020b)
HATS 551-021	138	$^{+15}_{-5}$	1.53	$^{+0.06}_{-0.08}$	3.64	0.06	⋯	1.10	0.10	1.20	$^{+0.08}_{-0.01}$	6670	220	Zhou et al. (2014a)
EBLM J2017 + 02	142.2	$^{+6.6}_{-6.7}$	1.489	$^{+0.127}_{-0.097}$	0.822	0[a]	⋯	1.105	$^{+0.074}_{-0.072}$	1.196	$^{+0.080}_{-0.050}$	6161	124	von Boetticher et al. (2019)
KIC 1571511	148.0	0.5	1.735	$^{+0.005}_{-0.006}$	14.02	0.3269	0.0027	1.265	$^{+0.036}_{-0.030}$	1.343	$^{+0.012}_{-0.010}$	6195	50	Ofir et al. (2012)
WTS 19g-4-02069	150	6	1.69	0.06	2.44	0[a]	⋯	0.53	0.02	0.51	0.01	3300	140	Nefs et al. (2013)
K2-51	152.8	$^{+3.4}_{-3.0}$	1.656	$^{+0.031}_{-0.045}$	13.001	0.3797	$^{+0.0090}_{-0.0058}$	1.068	$^{+0.032}_{-0.029}$	1.695	$^{+0.037}_{-0.049}$	5908	$^{+63}_{-64}$	Shporer et al. (2017)
TIC 238855958	155.0	3.1	1.664	0.029	38.195	0.298		1.514	0.037	2.159	0.037	6280	85	Gill et al. (2020a)
K2-67	168.9	$^{+7.0}_{-7.5}$	1.942	$^{+0.065}_{-0.116}$	24.388	0.36	$^{+0.018}_{-0.016}$	0.916	$^{+0.290}_{-0.031}$	1.399	$^{+0.056}_{-0.079}$	5579	$^{+78}_{-77}$	Shporer et al. (2017)
EBLM J0543-56	171.9	$^{+6.0}_{-6.2}$	1.877	$^{+0.097}_{-0.068}$	4.464	0[a]	⋯	1.276	$^{+0.072}_{-0.070}$	1.255	$^{+0.054}_{-0.036}$	6223	124	von Boetticher et al. (2019)
HATS 551-019	178	10	1.79	0.10	4.69	0.04	⋯	1.10	$^{+0.05}_{-0.09}$	1.70	0.09	6380	170	Zhou et al. (2014a)
KIC 7605600	178	11	1.94	$^{+0.01}_{-0.02}$	3.326	0.0013	$^{+0.0043}_{-0.0008}$	0.53	0.02	0.501	$^{+0.001}_{-0.002}$	⋯	⋯	Han et al. (2019)
EBLM J1038-37	181.8	$^{+6.9}_{-7.0}$	1.995	$^{+0.107}_{-0.097}$	5.022	0[a]	⋯	1.176	$^{+0.072}_{-0.070}$	1.132	$^{+0.052}_{-0.048}$	5885	124	von Boetticher et al. (2019)
EBLM J2349-32	182.3	6.3	1.966	0.049	3.5496972	0.001	0.002	0.991	0.049	0.965	0.022	6130	85	Gill et al. (2019)
EBLM J1013 + 01	185.7	$^{+7.9}_{-8.1}$	2.092	0.058	2.892	0[a]	⋯	1.036	$^{+0.070}_{-0.072}$	1.036	$^{+0.027}_{-0.026}$	5579	124	von Boetticher et al. (2019)
EBLM J1115-36	187.4	$^{+6.4}_{-6.2}$	1.877	$^{+0.078}_{-0.058}$	10.543	0.0522	$^{+0.0038}_{-0.0037}$	1.369	0.072	1.579	$^{+0.048}_{-0.041}$	6605	124	von Boetticher et al. (2019)
HATS 551-027	187.5	$^{+2.1}_{-1.0}$	2.121	$^{+0.068}_{-0.107}$	4.077	0.002	⋯	0.244	0.003	0.261	$^{+0.006}_{-0.009}$	3190	100	Zhou et al. (2015)
EBLM J2308-46	190.7	5.2	1.839	0.049	2.199187	0.009	0.011	1.223	0.049	1.534	0.041	6185	85	Gill et al. (2019)
J0113 + 31	194.9	10.5	2.033	0.107	14.28	0.3098	0.0005	0.945	0.045	1.378	0.058	5961	54	Gómez Maqueo Chew et al. (2014)
2MASS J0446 + 19	199	21	2.04	0.10	0.62	0[a]	⋯	0.47	0.05	0.56	0.02	3320	150	Hebb et al. (2006)
T-Lyr-101662	207	13	2.32	0.07	4.23	0.037	0.01	0.77	0.08	1.14	0.03	6200	30	Fernandez et al. (2009)
HATS 553-001	209	$^{+11}_{-21}$	2.19	0.10	3.8	0.03	⋯	1.20	0.10	1.58	$^{+0.08}_{-0.03}$	6230	250	Zhou et al. (2014a)
AD 3814	211.8	4.7	2.195	$^{+0.061}_{-0.048}$	6.02	0.00194	$^{+0.00253}_{-0.00057}$	0.3813	0.0074	0.3610	0.0033	3211	$^{+54}_{-36}$	Gillen et al. (2017)
Kepler-16	212.2	0.7	2.201	0.006	41.08	0.15944	$^{+0.00062}_{-0.00061}$	0.6897	$^{+0.0035}_{-0.0034}$	0.6489	0.0013	4450	150	Doyle et al. (2011)
EBLM J0339 + 03	215.9	$^{+9.7}_{-10.0}$	2.014	$^{+0.117}_{-0.100}$	3.581	0[a]	⋯	1.036	$^{+0.074}_{-0.076}$	1.210	$^{+0.055}_{-0.052}$	6132	124	von Boetticher et al. (2019)
OGLE-TR-125	219	35	2.05	0.26	5.3	0	0.01	⋯	⋯	1.94	0.18	⋯	⋯	Pont et al. (2005b)
PTFEB132.707 + 19.810	219.8	1.5	2.647	0.117	6.016	0.0017	0.0006	0.3953	0.0020	0.363	0.008	3260	67	Kraus et al. (2017)

Note.
[a] Eccentricity fixed at 0.

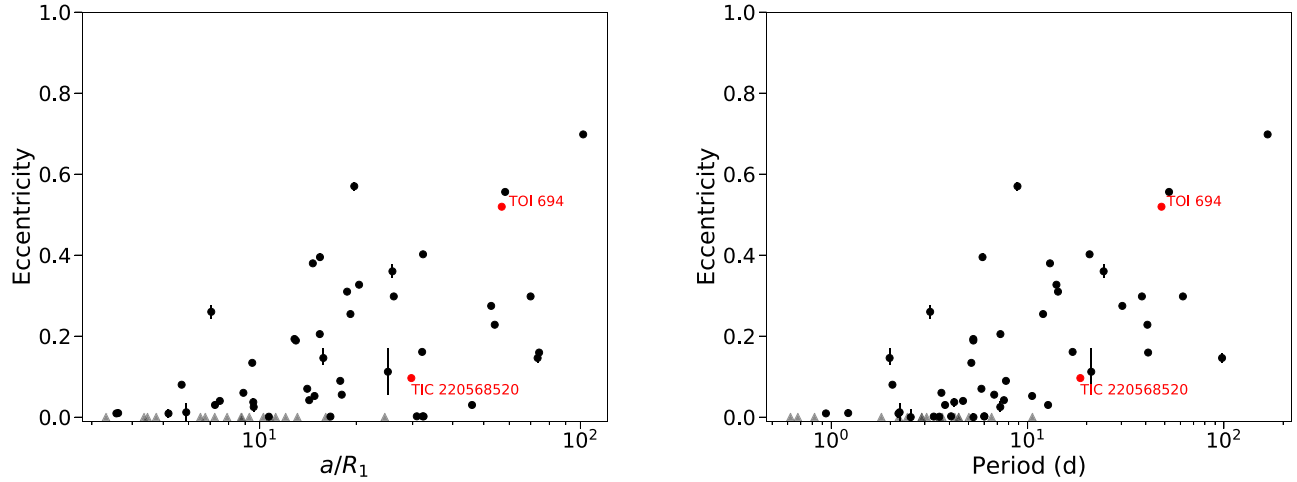

Figure 11. Eccentricity as a function of scaled semimajor axis (left) and period (right) for the substellar and stellar companions listed in Table 4. The scaled semimajor axis for each system is determined using Kepler's Third Law. The two systems studied here are labeled and marked in red. Error bars are plotted for all systems, but for some they are smaller than the size of the marker. Faded triangles represent systems where the eccentricity was fixed to 0.

(Hut 1981; Zimmerman et al. 2017), the rotation periods would be longer than the typical few days orbital periods of most of the systems in Table 4. Therefore, whether or not enhanced magnetic fields affect the radius of low-mass stars, it is not likely that they affect the radius of the two low-mass stars studied here.

Both systems studied here have a non-circular orbit, with well-measured orbital eccentricity. That is expected given their relatively long orbital periods, leading to a predicted orbital circularization timescale on the order of 10^{14}–10^{15} yr (Hilditch 2001). We show in Figure 11 the orbital eccentricity as a function of scaled semimajor axis and orbital period for all of the systems with brown dwarfs and low-mass stellar secondaries listed in Table 4. The figure shows TIC 220568520 with an eccentricity at the lower end of the eccentricity range of systems with similar orbital periods, and TOI 694 with an eccentricity close to the upper end of that of systems at similar orbital periods.

Tidal alignment for well separated binaries occurs on a similar timescale as tidal synchronization (Hut 1981). For the two systems studied here, the synchronization timescales are on the order of 10^{12} yr, meaning that these systems are not expected to be aligned due to tidal alignment mechanisms, although, they may have formed in aligned configurations. Therefore, measuring the primary star's obliquity, through the Rossiter–McLaughlin (RM) effect (e.g., Albrecht et al. 2007; Gaudi & Winn 2007; Triaud 2018), can probe their formation process (e.g., Pringle 1989; Bonnell et al. 1992; Bonnell 1994; Fabrycky & Tremaine 2007). The predicted semi-amplitudes of the RM RV signal are 17 m s^{-1} and 35 m s^{-1} for TOI 694 and TIC 220568520, respectively (derived using Equation (1) of Triaud 2018).

The well-measured orbits and transits allow us to calculate the expected phase and duration of the secondary eclipses, where the low-mass star moves behind the primary star. A detection of a secondary eclipse and a measurement of its depth can constrain the temperature of the low-mass object, leading to a more complete characterization. The phase-folded light curves of TOI 694 and TIC 220568520 during secondary eclipse phase are plotted in the right panels of Figures 2 and 4, respectively. For each object we calculated the mean and standard deviation (root mean square) of all measurements determined to be within the secondary eclipse while removing 5σ outliers. For TOI 694 the measured secondary eclipse depth of the binned 2 minute cadence data is -75 ± 1164 ppm, and for TIC 220568520 it is 190 ± 811 ppm. While these are obviously non-detections, they are consistent with the expected TESS-band shallow secondary eclipses given the expected effective temperatures of the small low-mass companions. By assuming blackbody spectra and integrating across the TESS band we derive an expected secondary eclipse depth of ≈300 ppm for TOI 694 assuming its effective temperature is 2600 K, and ≈580 ppm for TIC 220568520 assuming its effective temperature is 2800 K.

While the secondary eclipses are not detected in TESS data and are too shallow to be detected from the ground in visible light, they are expected to be deeper, and perhaps detectable, in longer wavelengths. For example, in the *K*-band (centered around 2.1 μm) the expected depths are ≈2300 ppm and ≈3900 ppm, for TOI 694 and TIC 220568520, respectively. More broadly, a comparison between the expected secondary eclipse depths and the uncertainty of the measured secondary eclipse depths (see previous paragraph) shows that for similar objects but with shorter orbital periods (and hence longer eclipses in phase) and brighter primary stars the noise level can potentially allow a detection of the secondary eclipse for low-mass stars.

5. Summary

We presented the discovery of two low-mass stars that are transiting (eclipsing) binary companions to Sun-like stars with eccentric orbits. The two low-mass stars are at the very bottom of the main sequence, close to and above the hydrogen-burning mass threshold. They join a short but growing list of low-mass stars with well-measured mass and radius. The relatively long orbital period of both systems means that the low-mass stars' radius is not likely to be impacted by enhanced magnetic fields, and we find their position in the radius–mass diagram to be consistent with theoretical models.

These discoveries emphasize the potential of transit surveys for detecting rare transiting low-mass binary companions, since given the similarity in radius of objects between ∼1 Jupiter-mass gas-giant planets through ∼100 Jupiter-mass stars, transiting gas-giant planet candidates are also, by definition,

low-mass star candidates. During the TESS Extended Mission the two targets studied here will be observed again, leading to a refined transit light-curve measurement and tighter upper limits on the secondary eclipse or possibly a secondary eclipse detection.

We acknowledge the use of TESS Alert data. These data are derived from pipelines at the TESS Science Office and at the TESS Science Processing Operations Center. Funding for the TESS mission is provided by NASA's Science Mission directorate. This paper includes data collected by the TESS mission, which are publicly available from the Mikulski Archive for Space Telescopes (MAST). Resources supporting this work were provided by the NASA High-End Computing (HEC) Program through the NASA Advanced Supercomputing (NAS) Division at Ames Research Center. This research has made use of the NASA Exoplanet Archive, which is operated by the California Institute of Technology, under contract with NASA under the Exoplanet Exploration Program. This work has been carried out within the framework of the National Centre of Competence in Research PlanetS supported by the Swiss National Science Foundation. M.N.G. acknowledges support from MIT's Kavli Institute as a Torres postdoctoral fellow. L.A.dS. is supported by funding from the European Research Council (ERC) under the European Union's Horizon 2020 research and innovation program (project FOUR ACES; grant agreement No 724427). A.J. acknowledges support from FONDECYT project 1171208 and by the Ministry for the Economy, Development, and Tourism's Programa Iniciativa Científica Milenio through grant IC 120009, awarded to the Millennium Institute of Astrophysics (MAS).

Facilities: TESS, ANU:2.3 m (Echelle), Euler 1.2 m (CORALIE) MPG/ESO:2.2 m (FEROS), SMARTS:1.5 m (CHIRON), SOAR (HRCam).

ORCID iDs

Ismael Mireles https://orcid.org/0000-0002-4510-2268
Avi Shporer https://orcid.org/0000-0002-1836-3120
Nolan Grieves https://orcid.org/0000-0001-8105-0373
George Zhou https://orcid.org/0000-0002-4891-3517
Rafael Brahm https://orcid.org/0000-0002-9158-7315
Carl Ziegler https://orcid.org/0000-0002-0619-7639
Keivan G. Stassun https://orcid.org/0000-0002-3481-9052
Chelsea X. Huang https://orcid.org/0000-0003-0918-7484
Stéphane Udry https://orcid.org/0000-0001-7576-6236
Michael Ireland https://orcid.org/0000-0002-6194-043X
Paula Sarkis https://orcid.org/0000-0001-8128-3126
Andrés Jordán https://orcid.org/0000-0002-5389-3944
Nicholas Law https://orcid.org/0000-0001-9380-6457
Andrew W. Mann https://orcid.org/0000-0003-3654-1602
Wei-Chun Jao https://orcid.org/0000-0003-0193-2187
Todd J. Henry https://orcid.org/0000-0002-9061-2865
Joseph E. Rodriguez https://orcid.org/0000-0001-8812-0565
Liang Yu https://orcid.org/0000-0003-1667-5427
Erin Flowers https://orcid.org/0000-0001-8045-1765
George R. Ricker https://orcid.org/0000-0003-2058-6662
David W. Latham https://orcid.org/0000-0001-9911-7388
Roland Vanderspek https://orcid.org/0000-0001-6763-6562
Joshua N. Winn https://orcid.org/0000-0002-4265-047X
Jon M. Jenkins https://orcid.org/0000-0002-4715-9460
Katharine Hesse https://orcid.org/0000-0002-2135-9018
Mark E. Rose https://orcid.org/0000-0003-4724-745X
Jeffrey C. Smith https://orcid.org/0000-0002-6148-7903
Daniel A. Yahalomi https://orcid.org/0000-0003-4755-584X
Zhuchang Zhan https://orcid.org/0000-0002-4142-1800

References

Albrecht, S., Reffert, S., Snellen, I., et al. 2007, A&A, 474, 565
Andersen, M., Meyer, M. R., Greissl, J., et al. 2008, ApJL, 683, L183
Baraffe, I., Chabrier, G., Barman, T. S., et al. 2003, A&A, 402, 701
Baraffe, I., Homeier, D., Allard, F., et al. 2015, A&A, 577, A42
Bayliss, D., Hojjatpanah, S., Santerne, A., et al. 2017, AJ, 153, 15
Beatty, T. G., Fernández, J. M., Latham, D. W., et al. 2007, ApJ, 663, 573
Bonnell, I., Arcoragi, J.-P., Martel, H., et al. 1992, ApJ, 400, 579
Bonnell, I. A. 1994, MNRAS, 269, 837
Bonnell, I. A., Larson, R. B., & Zinnecker, H. 2007, in Protostars and Planets V, ed. B. Reipurth, D. Jewitt, & K. Keil (Tucson, AZ: Univ. Arizona Press), 149
Bonomo, A. S., Sozzetti, A., Santerne, A., et al. 2015, A&A, 575, A85
Bouchy, F., Deleuil, M., Guillot, T., et al. 2011, A&A, 525, A68
Brahm, R., Espinoza, N., Jordán, A., et al. 2019, AJ, 158, 45
Brahm, R., Jordán, A., & Espinoza, N. 2017, PASP, 129, 034002
Buchhave, L. A., Latham, D. W., Johansen, A., et al. 2012, Natur, 486, 375
Burrows, A., Heng, K., & Nampaisarn, T. 2011, ApJ, 736, 47
Cañas, C. I., Bender, C. F., Mahadevan, S., et al. 2018, ApJL, 861, L4
Carmichael, T. W., Latham, D. W., & Vanderburg, A. M. 2019, AJ, 158, 38
Carmichael, T. W., Quinn, S. N., Mustill, A. J., et al. 2020, AJ, 160, 53
Castelli, F., & Hubrig, S. 2004, A&A, 425, 263
Chabrier, G. 2003, PASP, 115, 763
Chabrier, G., Gallardo, J., & Baraffe, I. 2007, A&A, 472, L17
Chaturvedi, P., Chakraborty, A., Anandarao, B. G., et al. 2016, MNRAS, 462, 554
Choi, J., Dotter, A., Conroy, C., et al. 2016, ApJ, 823, 102
Claret, A. 2017, A&A, 600, A30
Csizmadia, S., Hatzes, A., Gandolfi, D., et al. 2015, A&A, 584, A13
Cutri, R. M., Skrutskie, M. F., van Dyk, S., et al. 2003, yCat, 2246, 0
David, T. J., Hillenbrand, L. A., Gillen, E., et al. 2019, ApJ, 872, 161
Deleuil, M., Deeg, H. J., Alonso, R., et al. 2008, A&A, 491, 889
Díaz, R. F., Damiani, C., Deleuil, M., et al. 2013, A&A, 551, L9
Díaz, R. F., Montagnier, G., Leconte, J., et al. 2014, A&A, 572, A109
Donati, J.-F., Semel, M., Carter, B. D., et al. 1997, MNRAS, 291, 658
Dotter, A. 2016, ApJS, 222, 8
Doyle, L. R., Carter, J. A., Fabrycky, D. C., et al. 2011, Sci, 333, 1602
Fabrycky, D., & Tremaine, S. 2007, ApJ, 669, 1298
Fernandez, J. M., Latham, D. W., Torres, G., et al. 2009, ApJ, 701, 764
Foreman-Mackey, D., Hogg, D. W., Lang, D., et al. 2013, PASP, 125, 306
Gaia Collaboration, Brown, A. G. A., Vallenari, A., et al. 2018, A&A, 616, A1
Gaudi, B. S., & Winn, J. N. 2007, ApJ, 655, 550
Gill, S., Bayliss, D., Cooke, B. F., et al. 2020a, MNRAS, 491, 1548
Gill, S., Cooke, B. F., Bayliss, D., et al. 2020b, MNRAS, 495, 2713
Gill, S., Maxted, P. F. L., Evans, J. A., et al. 2019, A&A, 626, A119
Gillen, E., Hillenbrand, L. A., David, T. J., et al. 2017, ApJ, 849, 11
Gómez Maqueo Chew, Y., Morales, J. C., Faedi, F., et al. 2014, A&A, 572, A50
Gould, A., Pepper, J., & DePoy, D. L. 2003, ApJ, 594, 533
Günther, M. N., & Daylan, T. 2019, Allesfitter: Flexible Star and Exoplanet Inference from Photometry and Radial Velocity, v1.1.0, Astrophysics Source Code Library, ascl:1903.003
Günther, M. N., & Daylan, T. 2020, arXiv:2003.14371
Han, E., Muirhead, P. S., & Swift, J. J. 2019, AJ, 158, 111
Hebb, L., Wyse, R. F. G., Gilmore, G., et al. 2006, AJ, 131, 555
Henden, A. A., Templeton, M., Terrell, D., et al. 2016, yCat, 2336, 0
Hilditch, R. W. 2001, An Introduction to Close Binary Stars (Cambridge: Cambridge Univ. Press)
Hodžić, V., Triaud, A. H. M. J., Anderson, D. R., et al. 2018, MNRAS, 481, 5091
Hut, P. 1981, A&A, 99, 126
Irwin, J., Buchhave, L., Berta, Z. K., et al. 2010, ApJ, 718, 1353
Irwin, J. M., Charbonneau, D., Esquerdo, G. A., et al. 2018, AJ, 156, 140
Jackman, J. A. G., Wheatley, P. J., Bayliss, D., et al. 2019, MNRAS, 489, 5146
Jenkins, J. M., Twicken, J. D., McCauliff, S., et al. 2016, Proc. SPIE, 9913, 99133E
Jordán, A., Brahm, R., Espinoza, N., et al. 2020, AJ, 159, 145
Kaufer, A., Stahl, O., Tubbesing, S., et al. 1999, Msngr, 95, 8

Kesseli, A. Y., Muirhead, P. S., Mann, A. W., et al. 2018, AJ, 155, 225
Kipping, D. M. 2013, MNRAS, 435, 2152
Kraus, A. L., Douglas, S. T., Mann, A. W., et al. 2017, ApJ, 845, 72
Krumholz, M. R. 2014, PhR, 539, 49
Li, J., Tenenbaum, P., Twicken, J. D., et al. 2019, PASP, 131, 024506
Lindegren, L., Hernández, J., Bombrun, A., et al. 2018, A&A, 616, A2
Mamajek, E. E., & Hillenbrand, L. A. 2008, ApJ, 687, 1264
Marsh, T. R. 1989, PASP, 101, 1032
Maxted, P. F. L. 2016, A&A, 591, A111
Mazeh, T. 2008, EAS, 29, 1
Montet, B. T., Johnson, J. A., Muirhead, P. S., et al. 2015, ApJ, 800, 134
Morton, T. D. 2015, Isochrones: Stellar Model Grid Package, v2.1, Astrophysics Source Code Library, ascl:1503.010
Moutou, C., Bonomo, A. S., Bruno, G., et al. 2013, A&A, 558, L6
Nefs, S. V., Birkby, J. L., Snellen, I. A. G., et al. 2013, MNRAS, 431, 3240
Nowak, G., Palle, E., Gandolfi, D., et al. 2017, AJ, 153, 131
Nutzman, P., & Charbonneau, D. 2008, PASP, 120, 317
Ofir, A., Gandolfi, D., Buchhave, L., et al. 2012, MNRAS, 423, L1
Parviainen, H., Gandolfi, D., Deleuil, M., et al. 2014, A&A, 562, A140
Paxton, B., Bildsten, L., Dotter, A., et al. 2011, ApJS, 192, 3
Paxton, B., Cantiello, M., Arras, P., et al. 2013, ApJS, 208, 4
Paxton, B., Marchant, P., Schwab, J., et al. 2015, ApJS, 220, 15
Pepe, F., Mayor, M., Rupprecht, G., et al. 2002, Msngr, 110, 9
Persson, C. M., Csizmadia, S., Mustill, A. J., et al. 2019, A&A, 628, A64
Pont, F., Bouchy, F., Melo, C., et al. 2005a, A&A, 438, 1123
Pont, F., Melo, C. H. F., Bouchy, F., et al. 2005b, A&A, 433, L21
Pont, F., Moutou, C., Bouchy, F., et al. 2006, A&A, 447, 1035
Pringle, J. E. 1989, MNRAS, 239, 361
Queloz, D., Mayor, M., Udry, S., et al. 2001, Msngr, 105, 1
Ribas, I. 2006, Ap&SS, 304, 89
Ricker, G. R., Winn, J. N., Vanderspek, R., et al. 2015, JATIS, 1, 014003
Saumon, D., & Marley, M. S. 2008, ApJ, 689, 1327
Schlegel, D. J., Finkbeiner, D. P., & Davis, M. 1998, ApJ, 500, 525
Shporer, A., Zhou, G., Vanderburg, A., et al. 2017, ApJL, 847, L18
Siverd, R. J., Beatty, T. G., Pepper, J., et al. 2012, ApJ, 761, 123
Smith, J. C., Stumpe, M. C., Van Cleve, J. E., et al. 2012, PASP, 124, 1000
Southworth, J., Hinse, T. C., Dominik, M., et al. 2009, ApJ, 707, 167
Stassun, K. G., Collins, K. A., & Gaudi, B. S. 2017, AJ, 153, 136
Stassun, K. G., Corsaro, E., Pepper, J. A., et al. 2018a, AJ, 155, 22
Stassun, K. G., Oelkers, R. J., Pepper, J., et al. 2018b, AJ, 156, 102
Stassun, K. G., & Torres, G. 2016, AJ, 152, 180
Stassun, K. G., & Torres, G. 2018, ApJ, 862, 61
Stumpe, M. C., Smith, J. C., Catanzarite, J. H., et al. 2014, PASP, 126, 100
Stumpe, M. C., Smith, J. C., Van Cleve, J. E., et al. 2012, PASP, 124, 985
Šubjak, J., Sharma, R., Carmichael, T. W., et al. 2020, AJ, 159, 151
Tal-Or, L., Mazeh, T., Alonso, R., et al. 2013, A&A, 553, A30
Tokovinin, A. 2018, PASP, 130, 035002
Tokovinin, A., Fischer, D. A., Bonati, M., et al. 2013, PASP, 125, 1336
Torres, G., Andersen, J., & Giménez, A. 2010, A&ARv, 18, 67
Triaud, A. H. M. J. 2018, in Handbook of Exoplanets, ed. H. Deeg & J. Belmonte (Cham: Springer), 2
Triaud, A. H. M. J., Hebb, L., Anderson, D. R., et al. 2013, A&A, 549, A18
von Boetticher, A., Triaud, A. H. M. J., Queloz, D., et al. 2019, A&A, 625, A150
Winn, J. N., Holman, M. J., Torres, G., et al. 2008, ApJ, 683, 1076
Zhou, G., Bakos, G. Á, Bayliss, D., et al. 2019, AJ, 157, 31
Zhou, G., Bayliss, D., Hartman, J. D., et al. 2014a, MNRAS, 437, 2831
Zhou, G., Bayliss, D., Hartman, J. D., et al. 2015, MNRAS, 451, 2263
Zhou, G., Bayliss, D., Penev, K., et al. 2014b, AJ, 147, 144
Ziegler, C., Tokovinin, A., Briceño, C., et al. 2020, AJ, 159, 19
Zimmerman, M. K., Thompson, S. E., Mullally, F., et al. 2017, ApJ, 846, 147